Available online at www.sciencedirect.com
ScienceDirect
Trans. Nonferrous Met. Soc. China 30(2020) 14−26
Transactions of Nonferrous Metals Society of China
www.tnmsc.cn

2024 aluminum alloy ultrahigh-strength sheet due to two-level nanostructuring under cryorolling and heat treatment

Stanislav KRYMSKIY, Oleg SITDIKOV, Elena AVTOKRATOVA, Michael MARKUSHEV

Institute for Metals Superplasticity Problems, Russian Academy of Sciences,
39 Khalturin str., Ufa 450001, Russia

Received 26 March 2019; accepted 10 November 2019

Abstract: The effect of rolling to a total effective strain of 2 at the liquid nitrogen temperature and subsequent natural and artificial aging on the structure and service properties of the pre-quenched hot-pressed 2024 aluminum alloy was investigated. Using optical and electron microscopy, and X-ray analysis, it was found that the cryorolling did not qualitatively change the type of the initial coarse-fibered microstructure, but produced a well-developed nanocell substructure inside fibers. Further aging led to decomposition of the preliminary supersaturated and work-hardened aluminum solid solution and precipitation of strengthening phases in the statically recovered and/or recrystallized matrix. As a result, the rolled and naturally aged alloy demonstrated the yield and ultimate tensile strengths (YS= 590 MPa, UTS=640 MPa) much higher than those in the pressed and T6-heat treated alloy at equal elongation to failure (El~6%). Artificial aging at a temperature less than conventional T6 route could provide the extra alloy strengthening and the unique balance of mechanical properties, involving enhanced strength (YS=610 MPa, UTS=665 MPa) and ductility (El ~10%), and good static crack resistance (the specific works for crack formation and growth were 42 and 18 kJ/m^2, respectively) and corrosion resistance (the intensity and depth of intercrystalline corrosion were 23% and 50 μm, respectively).

Key words: aluminum alloy; cryogenic rolling; heat treatment; nanostructure; mechanical behavior; intergranular corrosion

1 Introduction

New strengthening methods for metal materials have aroused much interest to straining at low homological (cryogenic) temperatures. Such processing of pure metals and solid solutions usually results in well-developed deformation structures, accompanied by strength enhancement at ambient temperature [1−3]. The latter is caused by structural hardening owing to three factors: grain refinement (Hall−Petch strengthening) [1−4], development of dislocation and subgrain structures (dislocation and substructure strengthening, accordingly) [1−6]. The recent investigations [1−3,7,8] also have shown a great potential of severe plastic deformation (with an effective strain >2−3) to process ultrafine-grained and nanostructured (having the (sub)grain/ phase size less than 1 and 0.1 μm, accordingly) metals and alloys with unique strength in the as-deformed condition, as well as unique balance of strength, ductility and toughness after further annealing [1−3]. That is why it was of great interest to evaluate the effectiveness of severe plastic deformation at cryogenic temperatures [5,6,9], particularly for the age- hardenable alloys to reveal the integrated effect of their nanostructuring in both matrix (grain) and second phase structures. In other words, an intense interest can be excited by studying the synergy effect on their structural and disperse hardening in the course of thermo-mechanical treatment that combines cryostraining and heat treatment. The present work is a review of

Corresponding author: Stanislav KRYMSKIY; Tel: +7(347)282-38-56; E-mail: stkr_imsp@mail.ru
DOI: 10.1016/S1003-6326(19)65176-9

the recent data on the structure−property analysis of this phenomenon for commercial middle-strength age-hardenable 2024 aluminum alloy obtained in Refs. [10−15].

2 Experimental

5 mm-thick plates cut out from a hot-pressed rod of commercial 2024 (Al−4.4Cu−1.4Mg−0.7Mn, wt.%) aluminum alloy were preliminarily solution treated at 505 °C, water quenched (condition Q) and then isothermally rolled to strain of ~2.0 at the liquid nitrogen temperature. After cryorolling (CR) they were naturally and artificially aged (CR+NA and CR+AA, respectively) at 20 °C up to 144 h and at 100−190 °C up to 48 h, accordingly. Some samples in the initial and rolled conditions were also T6 heat treated under the conventional regimes, i.e. water quenching at 505 °C and artificial aging at 190 °C for 12 h (T6 and CR+T6, respectively).

The alloy microstructure was examined by optical metallography, transmission and scanning electron microscopy (OM, TEM and SEM), and X-ray diffraction (XRD) methods. To create an optical contrast mechanically grinded and polished samples were etched with Keller's reagent. The objects for TEM and SEM analyses were prepared by the standard procedure of jet electro-polishing in 20% solution of nitric acid in methanol. The SEM and XRD studies were carried out on the rolling plane of the samples taken from the central part of the processed sheets. The XRD analysis was performed in the Cu K_α radiation with a wavelength (λ) of 1.54418 Å on a DRON-4-07 diffractometer operated at a voltage of 40 kV and current of 30 mA with a graphite monochromator on a diffracted beam. The sample was rotated by a step of 0.1°, and scanning time at each step was 4 s. The root-mean-square microdeformation of the crystal lattice ($\langle\varepsilon^2\rangle^{1/2}$) and the coherent domain size (D_{CDS}) were calculated by the full-profile analysis method [16] using the materials analysis using diffraction (MAUD) software [17]. The deviations do not exceed 0.001% and 5 nm, respectively. The dislocation density (ρ) was calculated as [18]

$$\rho = 2\sqrt{3}\langle\varepsilon^2\rangle^{1/2} / (D_{CDS}\boldsymbol{b}) \quad (1)$$

where $\boldsymbol{b}$ is the Burgers vector.

The structure parameters of the alloy matrix (grain boundary spectrum, average misorientation angle of grain boundaries, fraction of low and high-angle boundaries (LABs and HABs, respectively), grain and subgrain sizes, volume fraction of recrystallized grains) were determined by means of electron backscatter diffraction (EBSD) analysis using a TESCAN MIRA 3 LMH microscope with a field emission gun, an OXFORD HKL registration system and a CHANNEL 5 software. The procedure of data analysis and reconstruction of misorientation maps was based on the recommendations in Refs. [19,20]. The scanning area (raster) was not less than 200 × 150 points with two scanning steps of 500 and 70 nm. The LABs were attested as boundaries with a misorientation angle from 2° to 15°, and those of the HABs were more than 15°. The boundaries misoriented at less than 2° were not taken into consideration. The size of structural elements (cells, subgrains and grains) was measured by the line-intercept method with a number of intersections not less than 500, providing an error no more than 5%.

The room temperature yield and ultimate tensile strength (YS and UTS), and elongation to failure (El) were measured on flat samples with a gage part of 9 mm × 3 mm × 0.7 mm that were machined in parallel to the rolling direction. The specific works of static crack formation and growth (A_{cf} and A_{cg}) were estimated by the Kahn's method on the samples of 28 mm × 20 mm × 0.7 mm in size with longitudinal-transverse orientation. The microhardness (HV) was evaluated using a Vickers indenter with a load of 1 N and loading time of 10 s.

The alloy resistance to intergranular corrosion (IGC) was tested on the samples 40 mm × 30 mm × 0.7 mm held in 3% sodium chloride and 1% hydrochloric acid water solution during 24 h. The average depth and intensity of a corrosion attack were determined in the pressing/rolling direction by the SEM measurements along the contact surface−the cross section of a rod/sheet.

Some more details on the alloy processing and methods of analysis can be easily found in Refs. [10−15].

3 Results and discussion

3.1 Structure and phase changes under cryorolling

The OM, TEM, SEM(EBSD) and XRD

analyses have shown that the microstructure of the alloy matrix before cryorolling (in the pre-quenched condition) was partially recrystallized, consisting of fibrous grains of 100−200 μm, elongated in the pressing direction, and near 5% of equiaxed recrystallized grains of about 5 μm in diameter (Figs. 1(a, c, e, g)). Inside fibers a polygonized structure with subgrains of 5 μm and a moderate

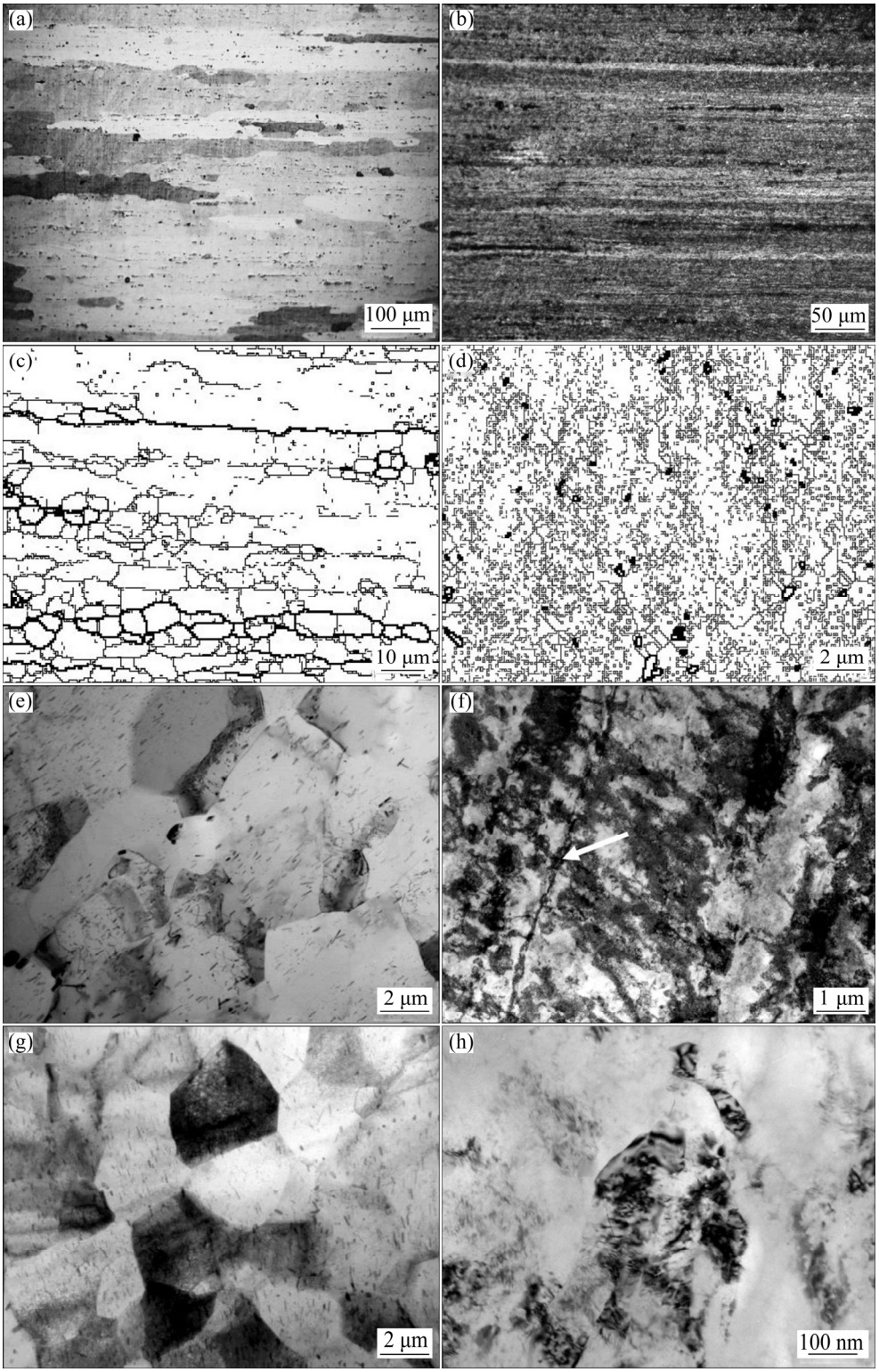

Fig. 1 OM (a, b), SEM−EBSD (c, d) and TEM (e−h) images of 2024 aluminum alloy in pre-quenched hot-pressed rod (a, c, e, g) and further cryorolled sheet (CR+NA) (b, d, f, h): (a, b, c, e) Longitudinal section of rod or sheet; (g) Cross section of rod; (d, f, h) Rolling plane of sheet (White arrow on (f) indicates “old” boundary of initial fiber. Hereafter, in EBSD maps LABs and HABs are indicated by grey and black lines, respectively)

density of lattice dislocations (ρ=8×10^{13} m^{-2}) (Table 1) was found. Thus, the grain boundary spectrum in this structure was bimodal with the average misorientation angle ~16º and fraction of HABs ~27%. Besides, the lattice of the matrix was characterized by a low level of microstress (0.09%) and a relatively large coherent domain size (~130 nm) (Table 1) [10−12,15].

Table 1 Crystal structure parameters of 2024 aluminum alloy

Condition	a/Å	D_{CDS}/ nm	$\langle\varepsilon^2\rangle^{1/2}$/ %	ρ/ 10^{14} m^{-2}
Q	4.0533± 0.0001	133±8	0.085± 0.005	0.8
T6	4.0512± 0.0001	127±11	0.089± 0.005	0.8
CR+NA	4.0487± 0.0001	60±4	0.344± 0.005	7.0
CR+AA (100 °C, 12 h)	4.0508± 0.0001	63±12	0.203± 0.003	4.0
CR+AA (190 °C, 12 h)	4.0496± 0.0001	86±8	0.109± 0.003	1.5

In spite of severe straining, the CR did not qualitatively change the type of the alloy microstructure, which remained predominantly fibrous (Fig. 1(b)). The CR led to further elongation of fibers, and decrease in their thickness to 10−20 μm, which was accompanied by substitution of the hot-pressed substructure with a well-developed, non-equilibrium cellular one with a cell size of 400−500 nm, and by one order increase in the dislocation density up to 7×10^{14} m^{-2} (Figs. 1(d, f)) [10−15]. Besides, the CR alloy was characterized by the same volume fraction of coarse excess phases as in starting material, meanwhile, their size was few times less and they were more homogeneously distributed in the sheet volume, owing to strain-induced brittle cracking under rolling.

Concerning the dynamic nanostructuring of the alloy, the TEM and SEM observations have demonstrated an insignificant fraction (1%−2%) of separate nanosized (sub)grains of about 130 nm in diameter (Fig. 1(h)), exhibiting a TEM contrast typical of non-equilibrium nanocrystallites obtained in aluminum alloys by other deformation techniques, for instance, by high pressure torsion [21]. However, the CR processed structure of the matrix surely can be considered as nanostructure with a determining structural parameter of the cell size (or even coherent domain size (Table 1)), which is a quite frequent practice in many studies [22−24].

Another nanostructural feature of the cryorolled alloy could be attributed with the second phases, especially with the secondary strengthening phases: precipitates of Mn-rich T-phase ($Al_{20}Cu_2Mn_3$) and Cu-rich S(Al_2CuMg) and θ(Al_2Cu) phases. Therewith, TEM, SEM and XRD analyses have revealed insignificant changes in the alloy phase composition due to the cryorolling. In spite of some decrease in the lattice parameter (Table 1), no visible observations of decomposition of the preliminary oversaturated aluminum solid solution and/or dissolution of any primary or secondary phases were found. Therefore, the alloy matrix after the CR was still oversaturated by Mg and Cu as in the pre-quenched state, and it was still strengthened by near homogeneously distributed T-phase precipitates ~120 nm × 60 nm in size, which formed during the alloy homogenization and further hot-pressing. As mentioned above, the only noticeable transformation in the alloy second phase structure under the CR was the size reduction and increase in the homogeneity of distribution of excess phases, which formed a banded structure in the hot-pressed rod. However, these particles were too coarse and of insignificant volume fraction to play any perceptible role in the structural changes of the alloy matrix, especially in its nanostructuring under rolling.

Taking into account the data published in Ref. [25], it should be considered that the microstructure of the pre-quenched and cryorolled to rather small strains alloy was qualitatively similar to that formed under conventional cold rolling. Meanwhile, the CR led to a strong decrease in some structural parameters, involving the coherent domain size, cell size, thickness of fibers and size of excess phases, and also resulted in a strong increase in the lattice microstrain and dislocation density (Table 1), indicating a highly non-equilibrium character of the processed structure. The latter factor could be the main cause of a lower value of the lattice parameter found in the CR alloy (Table 1).

3.2 Aging structure and response

After the natural and artificial aging at low

temperatures (up to ~100 °C), the structure of the CR alloy remained cellular with a mean cell/subgrain size of a bit less than 500 nm (Fig. 2). Under such aging, the main process of structure transformations was static recovery, resulting in insignificant changes in the volume fraction of nanograins [10,12−15].

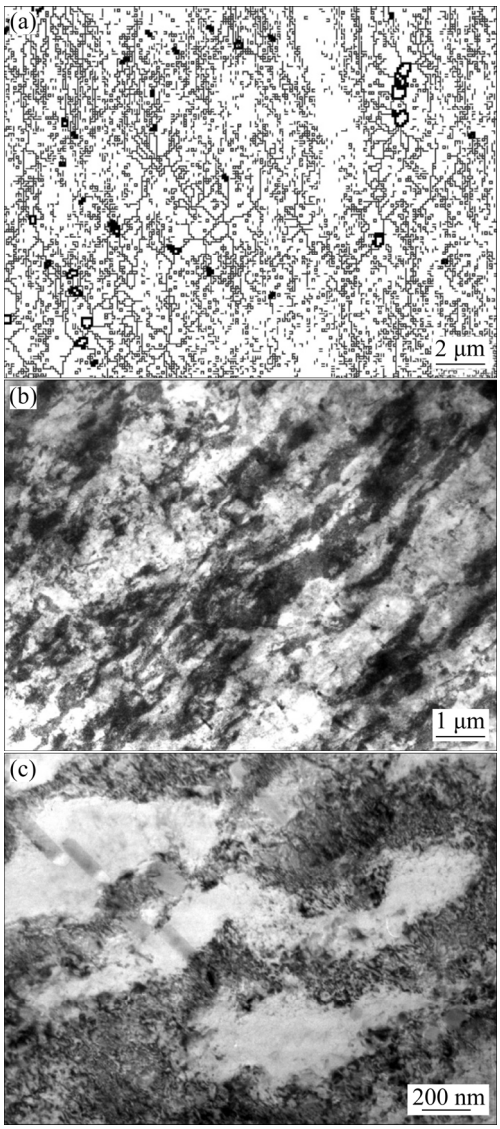

Fig. 2 SEM−EBSD (a) and TEM (b, c) images of 2024 aluminum alloy cryorolled and artificially aged at 100 °C for 12 h

Meanwhile, as in the non-rolled pre-quenched alloy, the decomposition of the aluminum solid solution will result in formation of the Guinier−Preston−Bagaryatsky (GPB) zones [26,27]. It is necessary to note that the observation of GPB zones as any disperse phases in a highly deformed matrix is a particularly hard challenge to solve especially by TEM. That is why, their existence and behavior were discussed mainly basing on the indirect measurements of the microhardness and its comparison with the microhardness and appropriate structure/phase transformations commonly observed in the starting material. Thus, the data presented in Fig. 3 testified that softening of the CR alloy under the matrix recovery upon room temperature annealing could be compensated by dispersion hardening only.

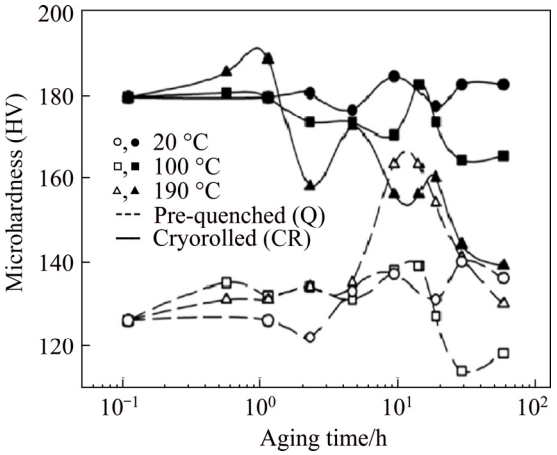

Fig. 3 Microhardness evolution in pre-quenched rod (Q) and further cryorolled (CR) 2024 aluminum alloy under aging at different temperatures

In spite of negligible changes in the alloy microstructure, the artificial aging at 100 °C, being too low for aging response of the non-rolled alloy, has resulted in the hardness decrease with aging time. Such behavior could be caused by a more intense than that at room temperature recovery of the deformation structure and decomposition of the aluminum solid solution, leading to faster precipitation and coagulation of the main strengthening phases, changing their morphology and densities toward the alloy softening [28,29].

The main feature of the matrix structure with the aging temperature increasing to 190 °C was its less homogeneity (Fig. 4), causing by the incompleteness of static recovery and recrystallization even at the long-term annealing. The higher fractions of deformation cells transformed into the areas with recovered subgrains and new recrystallized grains, increasing with aging time, the volume fraction of the nanocrystalline structure with equilibrium boundaries and grain bodies. Another feature was that the nanoprecipitates of different nature and morphology were formed inside of these cells, subgrains and

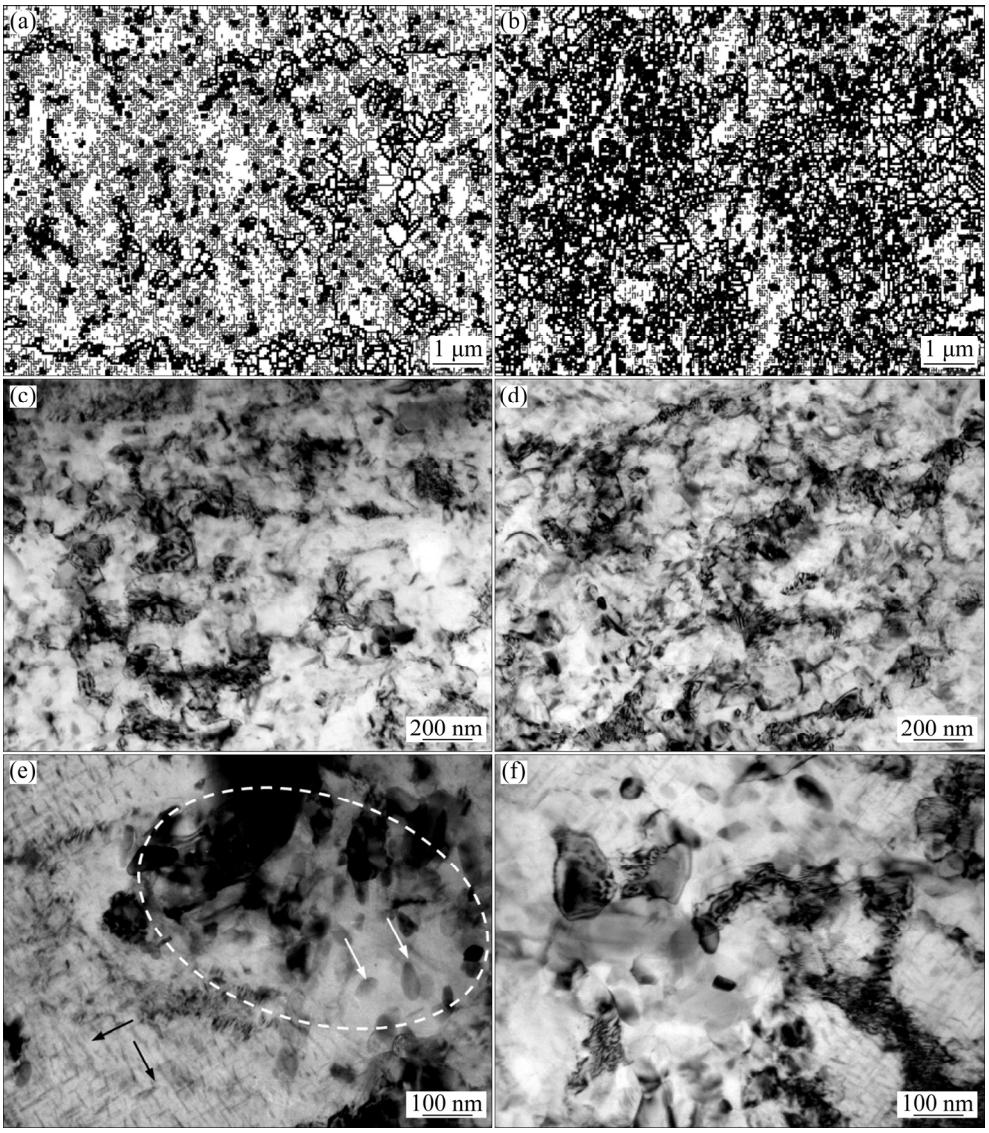

Fig. 4 SEM−EBSD (a, b) and TEM (c−f) images of cryorolled 2024 aluminum alloy after artificial aging at 190 °C for 12 h (a, c, e) and 48 h (b, d, f) (White circle indicates area with recrystallized nano-(sub)grain structure, black and white arrows-needle(disc)-like and compact *S*-phase precipitates, respectively)

recrystallized grains, and along their boundaries, (Fig. 4(e)). In general, such a two-level nanostructure can be considered as a bimodal one. The first mode is presented by a cell/dislocation structure with needle(disc)-like *S*-phase precipitates with a thickness of 2−10 nm and length up to ~100 nm (indicated by the black arrows in Fig. 4(e)), the second mode is nano/ultrafine (sub)grains with compact slightly elongated precipitates of 10−50 nm in size (indicated by the white circle and white arrows, respectively). The formation of such a structure can be discussed as follows. New intercrystalline boundaries formed during rolling served as the sites of preferential nucleation of precipitates. And increase in the diffusion rate along the cell boundaries and dislocation pipes ensured a higher rate of precipitate coagulation, leading to coarser and more compact secondary phases. On the other hand, faster decomposition of the Al solid solution and coarsening of precipitates during post-deformation annealing contributed to the acceleration of recovery and recrystallization, resulting in more rapid formation of an equilibrium (sub)grain structure. The latter, in turn, influenced the size, shape, and nature of precipitates leading to coarser precipitates of a compact shape instead of expected needle-like ones in the areas, where the recrystallization took place. At the same time, finer needle-like precipitates, which still existed in the

areas of the deformation structure, hindered the occurrence of recovery processes [10,12−15].

Therefore, the high-temperature artificial aging of the cryorolled alloy led to the formation of a multilevel nanostructure characterized by two nano-sized phase constituents, their specific volume fractions and morphology, a spectrum of grain and interphase boundaries. An increase in aging temperature and time led to faster softening of the CR alloy (Fig. 3) due to the simultaneous intensification of static recovery, continuous static recrystallization and decomposition of the aluminum solid solution [5,23,24].

Thus, an increase in the aging time to 48 h at 190 °C (corresponding to the conventional alloy conditions of overaging) resulted in an increase in the volume of recrystallized grains up to 50%−70% (Fig. 4(b)). The effect is also proved by the change in the lattice parameters of the alloy matrix upon annealing (Table 1). Thus, aging at 100 °C practically has no effect on the CR alloy lattice parameter and it significantly decreased at 190 °C, testifying a decrease in the Mg content in the matrix, and, consequently, intense and predominant precipitation of the strengthening *S*-phase [26].

It is also necessary to note that the strong suppression of the dynamic recovery under rolling resulted in the alloy dislocation density increase by near an order of magnitude (Table 1). Its decrease at further artificial aging was conditioned by activation of static recovery and recrystallization. It was, surprisingly, so sharp at 190 °C, demonstrating the ability of the CR material to complete softening even under conventional T6 aging.

3.3 Mechanical behavior

The cryorolling and subsequent natural aging led to enhanced tensile strength parameters much exceeding those in the conventional T6 rod (Fig. 5(a), Table 2). Moreover, the elongation-to-failure was also quite high for so strengthened alloy. Such strength−ductility balance was conditioned by formation of the above described microstructure, realizing work hardening and structural strengthening effects. However, post-deformation aging at 190 °C for 12 h of the CR material resulted in a slight enhancement of the alloy ductility accompanied by significant strength decrease due to three factors: deep decomposition of the aluminum solid solution with intense

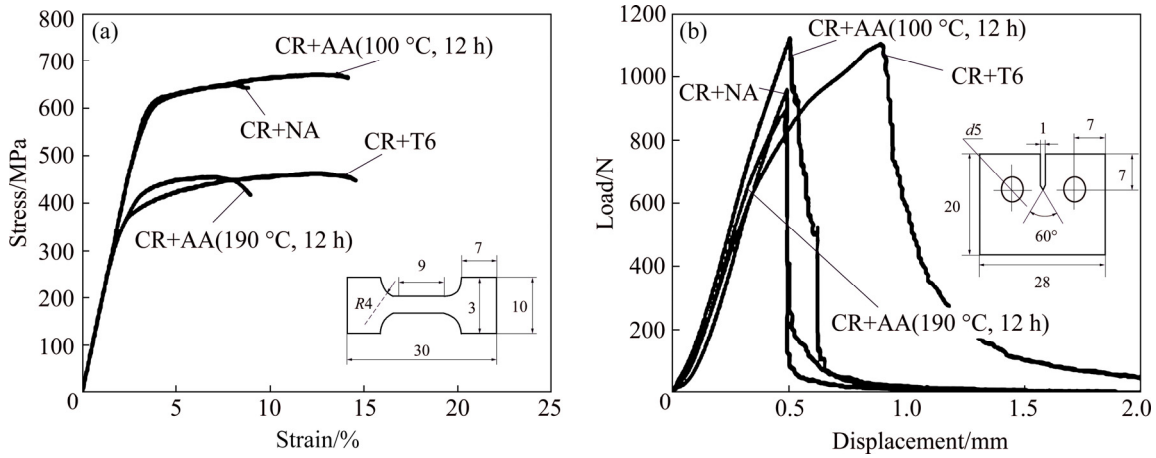

Fig. 5 Stress−strain (a) and load−displacement (b) curves under room temperature tension of cryorolled and heat treated 2024 aluminum alloy (Configurations of testing specimens used are shown in inserts, and all units are in mm)

Table 2 Mechanical and corrosion properties of 2024 aluminum alloy

Condition	YS/MPa	UTS/MPa	El/%	A_{cf}/(kJ·m^{-2})	A_{cg}/(kJ·m^{-2})	IGC depth/μm	IGC intensity/%
T6	390	440	7.0	–	–	–	–
CR+NA	590	640	5.9	27	4	35	14
CR+AA (190 °C, 12 h)	405	465	7.1	31	9	475	88
CR+AA (100 °C, 12 h)	610	665	10.4	42	18	50	23
CR+T6	375	465	12.0	138	46	525	50

coarsening of its products, as well as recovery and recrystallization of the matrix. These processes led to the formation of soft bimodal grain and precipitate structures, consisted of overaged plate-like *S*-phases in the recovered regions and coarser compact *S* and θ phases of lower densities in the recrystallized regions (Fig. 4). The correction of the aging regimes using AA at 100 °C could directly improve the situation, providing an unusual behavior for low-temperature severely deformed material, increasing both the alloy strength and ductility (Table 2). The latter could be conditioned by the formation of a predominantly recovered nanocellular structure with nanoscale plate-like metastable *S*-phase precipitates uniformly distributed along the elements of the dislocation structure.

At the same time it was found that the specific works of crack formation and growth in the cryorolled and naturally aged alloy were critically low, 27 and 4 kJ/m^2, especially the latter (Fig. 5(b), Table 2). This means that the alloy failure was near brittle owing to the sharp localization of crack initiation and growth. The artificial aging at 190 °C for 12 h can ensure a slight increase of both crack resistance parameters in spite of strong transformations of the alloy deformation micro-structure into a more equilibrium overaged one with quite coarse products of the aluminum solid solution decomposition. On the opposite, the aging at 100 °C for 12 h led to their enhancement by several times, 42 and 18 kJ/m^2, respectively. It should be noted that this level of crack resistance parameters is actually lower than that in the fully recrystallized T6 treated CR alloy (CR+ T6) [10,12−15]. However, it is sufficient for the efficient industrial applications of super-strengthened 2xxx alloy instead of, for instance, more expensive high-strength 7xxx series alloys.

Thus, the cryorolling and artificial aging via the non-conventional regimes could ensure a unique balance of tensile strength and crack resistance parameters obtained in the alloy, which demonstrates the strength values that were unachievable earlier, and only three times lower specific work of failure than that of the T6-treated alloy with a fully recrystallized coarse-grained structure. This effect is also caused by processing of the heterogeneous nano-(sub)grain structure strengthened by a mixture of nanoprecipitates (*T*- and *S*-type phases) formed at two structural levels to provide a specific combination of nano-sized main structure constituents, i.e., nanocrystallites and nanoprecipitates. This can be achieved by controlling the softening of severely deformed material under recovery and recrystallization of the deformation structure and simultaneously controlling the morphology and parameters of precipitates of strengthening phases, their size and distribution inside the alloy matrix under transformation.

3.4 Corrosion resistance

The analysis of the contact with corrosive media surfaces of the pre-quenched and naturally aged initial rod and CR sheet revealed that in both cases it could be described as commonly undamaged with numerical separate corrosion spots (Figs. 6(a) and (b) represented the typical features for CR alloy only). On the opposite, the well-defined and quite deep corrosion spots were observed in the T6 heat-treated conditions (Fig. 7). In spite of that the corrosion spots in the CR alloy were less homogeneously distributed and had dendrite-like shape (Figs. 7(c) and (d)), it could be concluded that in both cases the predominant IGC development was along the fiber boundaries and bands of excess phases.

The measurements have revealed that the IGC in the cryorolled and naturally aged alloy, unlike the initial naturally aged state, occurred with higher intensity and to higher depth (Fig. 8). At that time, the absolute values of these changes were not so high. The less corrosion resistance was found in the artificially aged conditions. The CR and conventionally artificially aged alloy has the worst corrosion resistance among the investigated ones. This means that cryorolling intensified the alloy corrosion by 1.7 times resulted in practically whole contact surface damage (Figs. 6−8) [12]. Meanwhile, the depth of its corrosion spots was a bit lower than that in the non-rolled T6-tempered rod. However, the behavior of the cryorolled and artificially aged alloy could be considerably improved, if the aging conditions were changed (Figs. 6(c) and (d)). Thus, the aging of the CR alloy treated at 100 °C for 12 h led to quite sensitive improvement of both IGC resistance parameters (Fig. 8) [12].

The alloy behavior observed could be

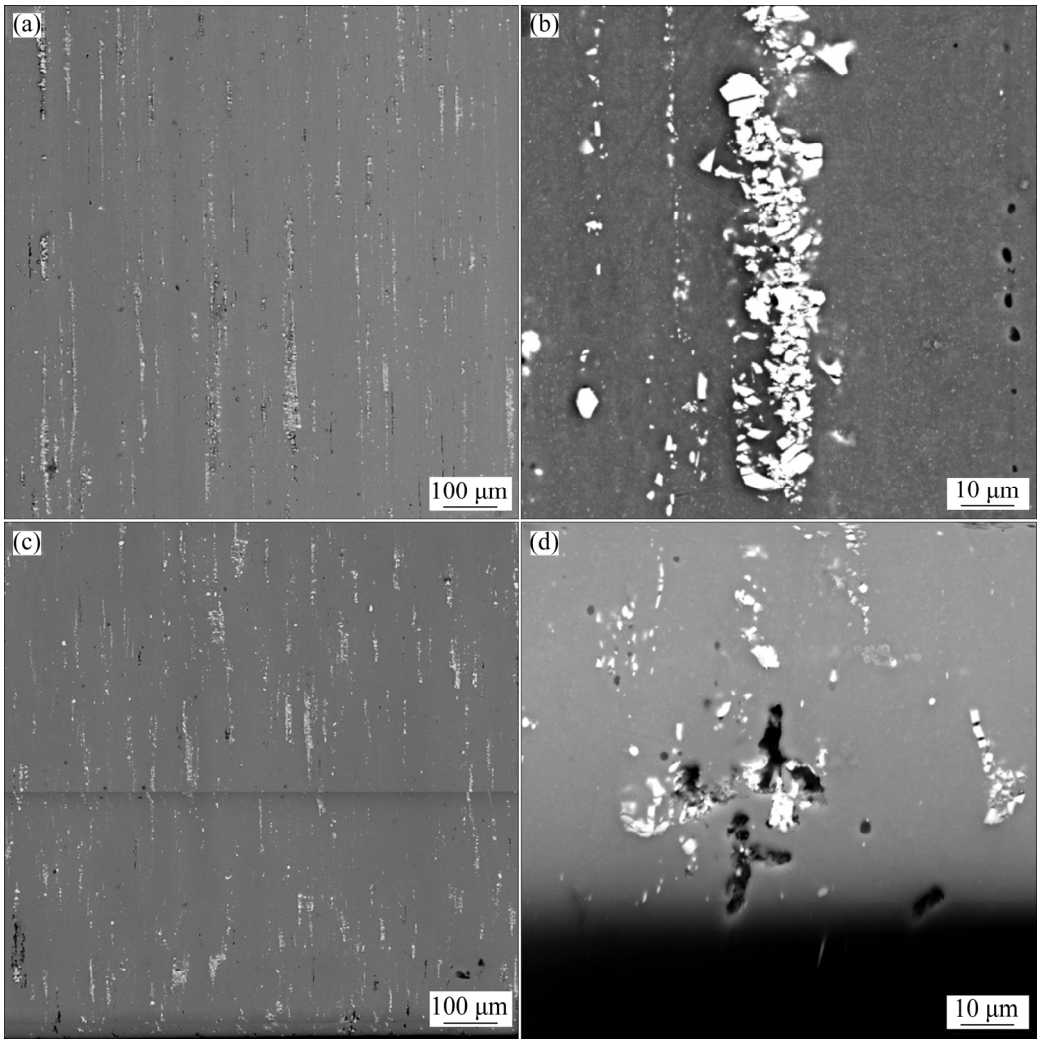

Fig. 6 Morphologies of 2024 aluminum alloy intergranular corrosion in cryorolled and naturally aged (a, b) and cryorolled and artificially aged at 100 °C for 12 h (c, d) conditions

explained by the following. It is well known that the main driving force for corrosion attack in 2xxx aluminum alloys is the difference in the electrochemical potentials of the volumes separated by different kinds of boundaries. The IGC predominantly develops along discrete and cathode paths to the alloy matrix, such as areas close to grain and interphase boundaries inside and between the aluminum solid solution and intermetallic particles and precipitates. Therewith, the more coherent with the matrix is the precipitate, the smaller is the difference between their lattices, and the lower is the IGC driving force. Also, the IGC penetrates through discontinuous anode areas, such as precipitate-free zones, which usually form under aging along high-angle boundaries [30−35]. Thus, the factors determining the corrosion behavior of aluminum alloys are commonly divided on the structural and phase ones.

The first group consists of factors, which are conditioned by the alloy matrix structure, the second group is the factors, which are impacted by second phases. Basing on the fact that during processing the both matrix and second phases were subjected to simultaneous changes, it can be considered that the corrosion attack, as other parameters of the alloy behavior, was synergy dependent on both factors. That is why, it is necessary to comprehensively explain their mutual influence.

Judging by the morphology of corrosion spots, irrespectively of the regimes of alloy processing, the main path of corrosion attack is the areas close to boundaries of fibers (Fig. 2) with bands of excess phases. As it was found, the cryorolling led to thinning and subdivision of fibers, decreasing the

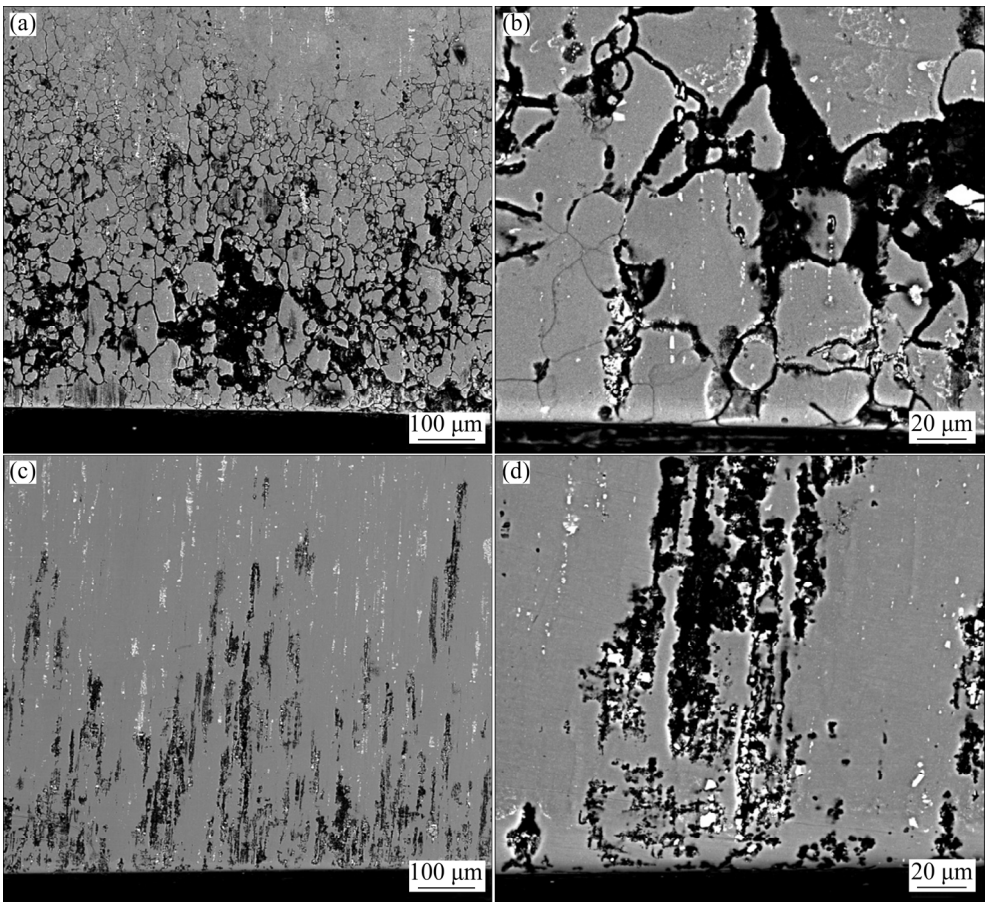

Fig. 7 Morphologies of 2024 aluminum alloy intergranular corrosion in pre-quenched and artificially aged (T6) hot-pressed rod (a, b) and cryorolled and artificially aged at 190 °C for 12 h (c, d) conditions

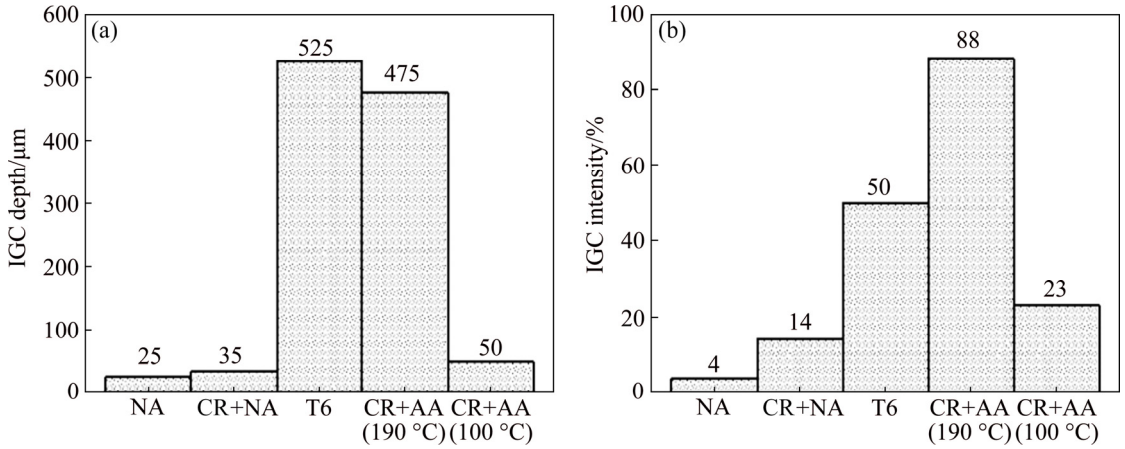

Fig. 8 2024 alloy intergranular corrosion depth (a) and intensity (b) in naturally and artificially aged initial hot-pressed rod and cryorolled sheet

distance between the bands of particles. Besides, the fibrous grains became narrower and with smaller interparticle spacing along and across their axis due to the mechanical rupture of initial coarse excess phases. As a result, the number density of particles along the fiber boundaries and on the cryorolled specimen contact surface was higher. Moreover, the cryorolling led to the increased density of crystal structure defects, mainly dislocations, and to the substitution of a hot-pressed (sub)structure by a more disperse and developed cell structure. Thus, by matching these facts and the data presented in Fig. 8, one may conclude, that all the listed changes in the structure of the naturally

aged alloy owing to cryorolling should intensify its corrosion. Such a point of view is also highlighted in a few papers. In Ref. [30], a decrease in the IGC resistance of cold-rolled steel was explained by the increased dislocation density, which resulted in the increased diffusion rate along dislocation pipes and, accordingly, intensified the corrosion spot. The enhancement of the IGC susceptibility as a result of fragmentation of excess phases in aluminum alloy was also shown in Ref. [32,33].

However, despite the fact that the above factors were responsible for the 2024 alloy behavior under processing involving cryorolling, they affected insignificantly its IGC resistance comparing to other factors. This is well seen by comparison of the data on both naturally aged (non-rolled and rolled) alloy conditions. Their annealing at ambient temperature can lead only to the formation of GPB zones. Due to the coherency of the crystalline lattices of the zone and the matrix, the difference in the electrochemical potential between them was low. Thus, irrespectively of the cryorolling, the formation of GPB zones did not affect significantly the intensity and depth of corrosion penetration (Fig. 8) [12].

As it was stated, in case of the artificial aging the main effect on the alloy IGC was caused by the aluminum solid solution decomposition with formation of metastable and stable phases. So, during aging of non-rolled alloy, semi-coherent plate-shape precipitates of the *S*-type phase formed, and the difference of the electro-chemical potential of the phase/matrix boundary increased, and a more intense IGC attack was caused, as compared with the naturally aged condition. The negative effect of cryorolling, which was expressed in a higher IGC intensity, was mainly indirect and conditioned by the synergy effect of the factors mentioned above and by the impact of recrystallization on the kinetics and sequence of the aging stages and on the morphology of its products (Fig. 4 and [13,14]). Namely, during the artificial aging of the CR alloy compact non-coherent precipitates of stable phases formed in the recrystallized areas, which apparently intensified the corrosion damage of the alloy.

4 Conclusions

(1) The isothermal rolling of the 2024 aluminum alloy at the liquid nitrogen temperature with a strain of 2 and subsequent natural aging retain the structure as coarse-grained with highly elongated fibrous grains and with the only nanosized parameter of the cell size.

(2) In spite of the absence of nanostructuring in terms of traditional approaches to grain refinement, the cryorolled and naturally aged alloy demonstrates a unique balance of the tensile strength parameters (YS=590 MPa, and UTS= 640 MPa), much higher than those in the conventionally T6 heat hardened products; the satisfied ductility (El=5.9%) and static crack formation and crack growth resistances (A_{cf}=27 kJ/m^2 and A_{cg}=4 kJ/m^2), as well as the relatively high resistance to intergranular corrosion.

(3) The post-rolling artificial aging activates the static recovery and recrystallization and, thus, results in simultaneous two-level nanostructuring with formation of a mixed nanoprecipitation strengthened nano-(sub)grain structure.

(4) The artificial aging according to the conventional regime (T6) led to the strength decrease of the cryorolled alloy roughly to common T6 values owing to elimination of crystal defects and alloy overaging. The use of new aging conditions led to the enhancement of all the tested alloy properties resulting in a unique balance of the alloy tensile strength (YS=610 MPa, UTS= 665 MPa), ductility (El=10.4%), crack resistance (A_{cf}=42 kJ/m^2 and A_{cg}=18 kJ/m^2) and sufficient corrosion resistance.

Acknowledgments

The present work was accomplished according to the state assignment of IMSP RAS (grant No. AAAA-A19-119021390107-8). Experimental studies were carried out on the facilities of shared services center of the Institute for Metals Superplasticity Problems of Russian Academy of Sciences “Structural and Physical-Mechanical Studies of Materials”.

References

[1] MA E. Eight routes to improve the tensile ductility of bulk nanostructured metals and alloys [J]. JOM, 2006, 58: 49−53. DOI: 10.1007/s11837-006-0215-5.

[2] ANDRIEVSKI R A, GLEZER A M, Strength of nanostructures [J]. Physics-Uspekhi, 2009, 52: 315−334. DOI: 10.3367/UFNe.0179.200904a.0337.

[3] MARKUSHEV M V, MURASHKIN M YU. Mechanical

properties of submicrocrystalline aluminum alloys after severe plastic deformation by angular pressing [J]. The Physics of Metals and Metallography, 2000, 90: 506−515.

[4] HUMPHREYS F J, HATHERLY M. Recrystallization and related annealing phenomena [M]. Oxford: Elsevier, 2004.

[5] YIN J, LU J, MA H, ZHANG P. Nanostructural formation of fine grained aluminium alloy by severe plastic deformation at cryogenic temperature [J]. Journal of Materials Science, 2004, 39, 2851−2854. DOI: 10.1023/B:JMSC.0000021463.83899.b3.

[6] ZHAO Y H, LIAO X Z, CHENG S, MA E, ZHU Y T. Simultaneously increasing the ductility and strength of nanostructured alloys [J]. Advanced Materials, 2006, 18: 2280−2283. DOI: 10.1002/adma.200600310.

[7] VALIEV R Z, ALEXANDROV I V. Nanostructural materials produced by severe plastic deformation [M]. Moscow: Logos, 2000. (in Russian)

[8] MARKUSHEV M V, VINOGRADOV A. Room temperature mechanical properties of submicrocrystalline commercial aluminum alloys processed by severe plastic deformation, in severe plastic deformation: Towards bulk production of nanostructured materials [M]. New York: Nova Science Publishers, 2006.

[9] KHAIMOVICH P A. Nanostructurization of metals cryodeformed at hydrostatic stress [J]. Russian Physics Journal, 2007, 50: 1079−1083. DOI: 10.1007/s11182-007-0158-5.

[10] KRYMSKIY S, SITDIKOV O, AVTOKRATOVA E, MURASHKIN M, MARKUSHEV M. Strength of cryorolled commercial heat hardenable aluminum alloy with multilevel nanostructure [J]. Reviews on Advanced Materials Science. 2012, 31: 145−150.

[11] KRYMSKIY S V, AVTOKRATOVA E V, SITDIKOV O SH, MIKHAYLOVSKAYA A V, MARKUSHEV M V. Structure of the aluminum alloy Al−Cu−Mg cryorolled to different strains [J]. Physics of Metals and Metallography, 2015, 116: 676−683. DOI: 10.1134/S0031918X15050105.

[12] KRYMSKIY S V, ILYASOV R R, AVTOKRATOVA E V, SITDIKOV O S H, MARKUSHEV M V. Intergranular corrosion of cryorolled and aged D16 aluminum alloy [J]. Protection of Metals and Physical Chemistry of Surfaces, 2017, 53: 1091−1099. DOI: 10.1134/S2070205117060144.

[13] MARKUSHEV M V, AVTOKRATOVA E V, KAZAKULOV I YA, KRYMSKIY S V, MOCHALOVA M YU, MURASHKIN M YU, SITDIKOV O SH. Microstructure and properties of an aluminum D16 alloy subjected to cryogenic rolling [J]. Russian Metallurgy (Metally), 2011, 4: 364−369. https://doi.org/10.1134/S0036029511040136.

[14] KRYMSKIY S V, AVTOKRATOVA E V, MARKUSHEV M V, MURASHKIN M YU, SITDIKOV O SH. Structure and hardness of cryorolled and heat-treated 2xxx aluminum alloy [J]. Materials Science Forum, 2011, 667−669: 925−930. https://doi.org/10.4028/www.scientific.net/MSF.667-669.925.

[15] AVTOKRATOVA E, KRYMSKIY S, MIKHAYLOVSKAYA A, SITDIKOV O, MARKUSHEV M. Nanostructuring of 2xxx aluminum alloy under cryorolling to high strains [J]. Materials Science Forum, 2016, 838−839: 367−372. https://doi.org/10.4028/www.scientific.net/MSF.838-839.367.

[16] SNYDER R L. Analytical profile fitting of X-ray powder diffraction profiles in Rietveld analysis [C]//YOUNG R A. The Rietveld Method. Oxford: Oxford University Press, 1993: 111−131.

[17] LUTTEROTTI L, MATTHIES S, WENK H R. MAUD (Material Analysis Using Diffraction): A user friendly Java program for Rietveld texture analysis and more [C]// Proceeding of the Twelfth International Conference on Textures of Materials (ICOTOM-12). 1999: 1599−1604. https://iris.unitn.it/handle/11572/57067?mode=full.16#.Xgy19-gzaM8.

[18] NOVIKOV I I, ROSIN K M. Crystallography and crystal-lattice defects [M]. Moscow: Metallurgiya, 1990. (in Russian)

[19] HUMPHREYS F J. Characterisation of fine-scale microstructures by electron backscatter diffraction (EBSD) [J]. Scripta Materialia, 2004, 51: 771−776. https://doi.org/10.1016/j.scriptamat.2004.05.016.

[20] SCHWARZER R A, FIELD D P, ADAMS B L, KUMAR M, SCHWARTZ A J. Present state of electron backscatter diffraction and prospective developments [C]//SCHWARTZ A J, KUMAR M, ADAMS B L L, FIELD D P. Electron Backscatter Diffraction in Materials Science. Berlin: Springer Science-Business Media, 2009: 1−20.

[21] MARKUSHEV M V, AVTOKRATOVA E V, KRYMSKIY S V, SITDIKOV O SH. Effect of precipitates on nanostructuring and strengthening of high-strength aluminum alloys under high pressure torsion [J]. Journal of Alloys and Compounds, 2018, 743: 773−779. https://doi.org/10.1016/j.jallcom.2018.02.047.

[22] KUMAR N, JAYAGANTHAN R, BROKMEIER H G. Effect of deformation temperature on precipitation, microstructural evolution, mechanical and corrosion behavior of 6082 Al alloy [J]. Transactions of Nonferrous Metals Society of China, 2017, 27: 475−492. DOI: 10.1016/S1003-6326(17)60055-4.

[23] ABBASI-BAHARANCHI M, KARIMZADEH F, ENAYATI M H. Thermal stability evaluation of nanostructured Al6061 alloy produced by cryorolling [J]. Transactions of Nonferrous Metals Society of China, 2017, 27: 754−762. DOI: 10.1016/S1003-6326(17) 60086-4.

[24] NIRANJANI V L, HARI KUMAR K C, SUBRAMANYA SARMA V. Development of high strength Al−Mg−Si AA6061 alloy through cold rolling and ageing [J]. Materials Science and Engineering A, 2009, 515: 169−174. https://doi.org/10.1016/j.msea.2009.03.077.

[25] LIU Q, HUANG X, LLOYD D J, HANSEN N. Microstructure and strength of commercial purity aluminum (AA 1200) cold-rolled to large strains [J]. Acta Materialia, 2002, 50: 3789−3802. https://doi.org/10.1016/S1359-6454(02)00174-X.

[26] MONDOLFO L F. Aluminium alloys: Structure and properties [M]. London: Butterworths, 1976.

[27] WANG S C, STARINK M J, GAO N. Precipitation hardening in Al−Cu−Mg alloys revisited [J]. Scripta Materialia, 2006, 54: 287−291. https://doi.org/10.1016/j.scriptamat.2005.09.010.

[28] HUANG Y, ROBSON J D, PRANGNELL P B. The formation of nanograin structures and accelerated room-

temperature theta precipitation in a severely deformed Al−4 wt.% Cu alloy [J]. Acta Materialia, 2010, 58: 1643−1657. https://doi.org/10.1016/j.actamat.2009.11.008.

[29] PANIGRAHI S K, JAYAGANTHAN R. Development of ultrafine grained high strength age hardenable Al 7075 alloy by cryorolling [J]. Materials & Design, 2011, 32: 3150−3160. https://doi.org/10.1016/j.matdes.2011.02.051.

[30] PEGUET L, MALKI B, BAROUX B. Influence of cold working on the pitting corrosion resistance of stainless steels [J]. Corrosion Science, 2007, 49: 1933−1948. DOI: 10.1016/j.corsci.2006.08.021.

[31] BRUNNER J G, MAY J, HOPPEL H W, GOKEN M, VIRTANEN S. Localized corrosion of ultrafine-grained Al−Mg model alloys [J]. Electrochimica Acta, 2010, 55: 1966−1970. https://doi.org/10.1016/j.electacta.2009.11.016.

[32] RALSTON K D, BIRBILIS N, DAVIES C H J. Revealing the relationship between grain size and corrosion rate of metals [J]. Scripta Materialia, 2010, 63: 1201−1204. https://doi.org/10.1016/j.scriptamat.2010.08.035.

[33] BALYANOV A, KUTNYAKOVA J, AMIRKHANOVA N A, STOLYAROV V V, VALIEV R Z, LIAO X Z, ZHAO Y H, JIANG Y B, XU H F, LOWE T C, ZHU Y T. Corrosion resistance of ultra fine-grained Ti [J]. Scripta Materialia, 2004, 51: 225−229. https://doi.org/10.1016/j.scriptamat.2004.04.011.

[34] CHUNG M K, CHOI Y S, KIM J G, LEE J C. Effect of the number of ECAP pass time on the electrochemical properties of 1050 Al alloys [J]. Materials Science and Engineering A, 2004, 366: 282−291. https://doi.org/10.1016/j.msea.2003.08.056.

[35] TSAI T S, CHUANG T H. Role of grain size on the stress corrosion cracking of 7475 aluminum alloys [J]. Materials Science and Engineering A, 1997, 255: 135−144. https://doi.org/10.1016/S0921-5093(96)10840-6.

深冷轧制和热处理获得具有二级纳米结构的 2024 铝合金超强板材

Stanislav KRYMSKIY, Oleg SITDIKOV, Elena AVTOKRATOVA, Michael MARKUSHEV

Institute for Metals Superplasticity Problems, Russian Academy of Sciences,
39 Khalturin str., Ufa 450001, Russia

摘　要：在液氮温度和应变为 2 条件下对预淬火热压 2024 铝合金进行轧制，研究轧制和后续天然和人工时效对其结构和服役性能的影响。利用光学显微镜、电子显微镜和 X 射线分析发现，深冷轧制并没有定性地改变最初粗纤维组织的类型，而是在纤维内部产生发育良好的纳米晶胞亚结构。进一步时效导致初步过饱和、加工硬化铝固溶体的分解，也导致静态回复和/或再结晶基体中强化相的沉淀。相比于压制和 T6 热处理态的合金，轧制和自然时效态的合金表现出更高的屈服强度(YS=590 MPa)和极限抗拉强度(UTS=640 MPa)，而两种合金的断裂伸长率相当(El~6 %)。低于常规 T6 路线温度的人工时效可以进一步提高合金的强度且保持良好的综合力学性能，包括较高的强度(YS=610 MPa, UTS=665 MPa)与延性(El~10%)、良好的静态裂纹阻力(裂纹形成和生长功分别为 42 和 18 kJ/m^2)和良好的耐腐蚀性(晶间腐蚀的强度和深度分别为 23%和 50 μm)。

关键词：铝合金；深冷轧制；热处理；纳米结构；力学行为；晶间腐蚀

(Edited by Xiang-qun LI)